AGU ADVANCING EARTH AND SPACE SCIENCE

Water Resources Research

RESEARCH ARTICLE
10.1029/2020WR029195

Modeling the Influence of a Variable Permeability Inclusion on Free-Surface Flow in an Inclined Aquifer

E. M. Hinton[1,2] and **A. J. Hogg**[1]

[1]School of Mathematics, Universtiy of Bristol, Bristol, United Kingdom, [2]School of Mathematics and Statistics, The University of Melbourne, Parkville, Australia

Key Points:

- We analyze a model of the interaction between free-surface flows and inclusions of different permeability in an inclined aquifer
- Simple descriptions are developed for the flow depth and streamlines in the regimes of relatively wide and relatively narrow inclusions
- Wider inclusions of different permeability to the exterior may divert the flow at the inclusion boundary, leading to deep ponded regions

Supporting Information:

Supporting Information may be found in the online version of this article.

Correspondence to:

E. M. Hinton,
ehinton@unimelb.edu.au

Citation:

Hinton, E. M., & Hogg, A. J. (2021). Modeling the influence of a variable permeability inclusion on free-surface flow in an inclined aquifer. *Water Resources Research*, *57*, e2020WR029195. https://doi.org/10.1029/2020WR029195

Received 8 NOV 2020
Accepted 5 MAR 2021

Abstract The interaction of sub-surface, gravity-driven flows with inclusions of different permeabilities are investigated theoretically using a model that exploits the relative shallowness of the motion. Numerically computed solutions for steady motion around cylindrical inclusions reveal a range of behaviors dependent on the ratio of the interior to exterior permeability and a dimensionless flow parameter that measures the far-field thickness to the product of the gradient of the slope down which the fluid flows and the width of the inclusion. When the inclusion is relatively narrow, the depth of the flow is little changed from its far-field value and the fluid is focused into inclusions of higher permeability and deflected around those of lower permeability. However, if the inclusion is relatively wide then three qualitatively different regimes emerge, dependent on the ratio of permeabilities. When the interior and exterior permeabilities are similar, then negligible deviation of the flow occurs apart from within thin transition layers at the boundary of the inclusion. When the permeabilities differ significantly, the flow forms deep ponds at either the upstream or downstream boundary of the inclusion for relatively low or high permeability inclusion, respectively, which arise due to deflection or focusing. In each case, asymptotic relationships are derived between the depth of the flow and the parameters. Inclusions of differing cross-section are also analyzed numerically and analytically to draw out the interplay between adjustment, deflection and focusing.

1. Introduction

Gravity-driven flows in porous media occur in a wide range of industrial and environmental contexts including hydrology, carbon dioxide storage, geothermal power generation, and contaminant leaks (Bear, 1971; Guo et al., 2016; MacFarlane et al., 1983). These sub-surface flows are difficult to monitor directly and therefore it is common to drill wells to sample the flow, for example in CO_2 storage projects to monitor breakthrough times (Hannis et al., 2015; Mathieson et al., 2011). Wells are also used for extracting fresh water from aquifers and for monitoring salt water intrusion (Barlow & Reichard, 2010; Dagan & Zeitoun, 1998; Masterson et al., 1998). Accurately determining the flow velocity from a single borehole presents difficulties, however, because its presence may significantly alter the flow field even in the case that no fluid is extracted because it alters the structure and permeability of the constituent porous media (Sekhar & Sano, 2001). It is vital to understand this effect in order to interpret the data acquired correctly.

It is well-established that pressure-driven flows are focused by inclusions that are of higher permeability than the surroundings whilst lower permeability inclusions divert the flow, and the volume flux of fluid that passes through the inclusion has been calculated in each case (Hinch & Bhatt, 1990; Phillips, 1991). However, in many contexts, the flow forms a free-surface and is primarily driven by buoyancy. We develop a physical model to explore the interaction of free-surface flows driven by gravity (rather than by imposed pressure gradients) on an inclined plane with a cylindrical inclusion of different permeability (Figure 1). We investigate how the flow thickness and velocity field depend on the permeability ratio and the width of the cylinder relative to the oncoming flow thickness and slope inclination. In the case of a relatively narrow cylinder, we show that the behavior is analogous to the interaction of two-dimensional pressure-driven flows with inclusions. The interaction with relatively wide cylinders is substantially different, however. For example, we will show that upstream of a relatively wide impermeable inclusion, deep ponds of fluid will form. Similar behavior occurs on the downstream side of the interior of a high permeability inclusion. We are particularly interested in the flux of fluid into the cylinder from upstream and determining controls on whether the particle paths are predominantly diverted around, focused into or not significantly influenced

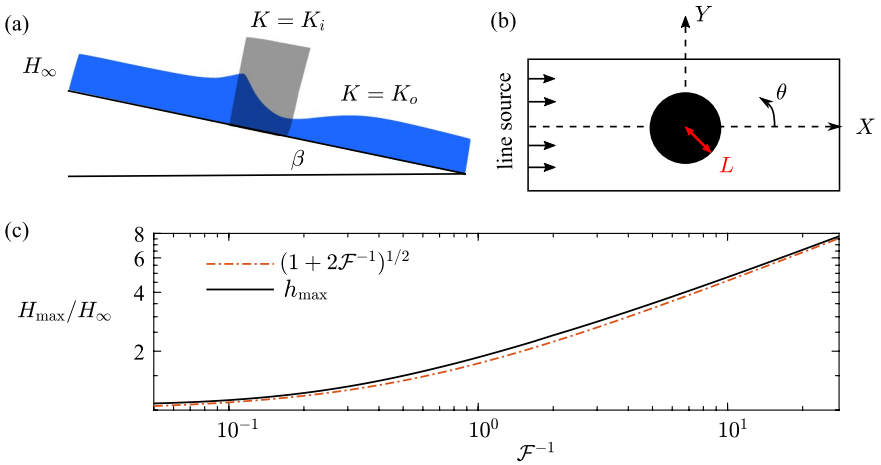

Figure 1. (a) Side view of the flow showing the far upstream thickness, H_∞. (b) Bird's eye view of the setup. (c) The maximum flow depth, $h_{\max} = H_{\max}/H_\infty$ as a function of the flow parameter, $\mathcal{F}$ for an impermeable circular cylinder.

by the cylindrical inclusion. Another aim is to determine the occurrence, depth and location of ponded regions in which the free-surface is approximately horizontal, the fluid is nearly stationary and the flow depth is much greater than its upstream value.

The present analysis has important applications for geologic CO_2 sequestration. The flow of the stored CO_2 is driven by buoyancy away from the injection well. The CO_2 is likely to contact abandoned wells, which may act as high or low permeability inclusions and Celia et al. (2005) showed that they could significantly influence the motion of the plume and present a key leakage risk (Nordbotten et al., 2004). In addition, the CO_2 may encounter natural heterogeneous inclusions owing to fractures in the rock, through which CO_2 may also leak (Pritchard, 2007; Woods & Norris, 2010). The CO_2 preferentially migrates through high permeability regions, which may increase the distance traveled and reduce the storage efficiency (Di Donato & Blunt, 2004).

Tracers are sometimes added to subsurface flows to monitor breakthrough times and constrain aquifer properties (Stalker et al., 2015) and rock heterogeneity is known to have a strong effect on the migration of tracers in a porous medium (Dagan, 1984; Werth et al., 2006). Indeed, it has been shown that inclusions of different permeability can totally dominate dispersion in a pressure-driven flow owing to the different speeds of particles that pass through the inclusion (Eames & Bush, 1999). In the context of free-surface flows, Hinton and Woods (2019) showed that vertical variations in permeability can lead to complex interactions between dispersing tracer and the interface. In this study, we use our results to calculate the paths taken as particles pass through and around the cylinder for the different flow regimes that occur depending on the relative permeability and width of the inclusion.

We begin our analysis in §2, where we formulate a shallow model for the flow using Darcy's law and we identify that the problem has two dimensionless parameters: the ratio of the permeabilities inside and outside a circular cylinder and the flow parameter, which is the ratio of the oncoming flow thickness to the product of the cylinder radius and the slope gradient. In §3, we consider the regime of a relatively narrow cylinder, which slightly perturbs the flow depth. Asymptotic predictions for the flow thickness inside and outside the cylinder are calculated. This identifies that if the cylinder has lower permeability than the surrounding medium then the flow is diverted around the cylinder and the maximum thickness occurs on the upstream boundary of the cylinder and the converse occurs for a cylinder of higher permeability.

We consider relatively wide obstructions in §4. In contrast to the "narrow" regime, the interaction with a wide obstruction is qualitatively sensitive to the permeability ratio. When this ratio is of order unity, the particle paths are parallel to the downslope direction passing straight through the cylinder. The velocity changes as particles enter the cylinder and mass conservation requires that the depth is constant outside the cylinder but a different constant inside the cylinder. However, if the cylinder is sufficiently impermeable (§5) then fluid ponds upstream of the cylinder. The oncoming flow is predominantly diverted around the

cylinder. This behavior is similar to the interaction of buoyant plumes with low permeability layers, which leads to lateral spreading before the fluid drains through the layer (Hewitt et al., 2020; Sahu & Flynn, 2017). In the case that the cylinder is of sufficiently high permeability relative to the exterior, the flow within the cylinder is focused toward a pond at the most downstream point (§6). The flow out of the cylinder occurs predominantly through this pond. In §7, we generalize the results to some cylinders with non-circular cross-sections to draw out some of the features that determine the location and magnitude of the ponds. We consider the implications of our results for some subsurface flows in §8. Concluding remarks are made in §9.

2. Formulation

We analyze the gravitationally driven steady flow of a fluid of dynamic viscosity μ in a saturated, deep porous medium, which is bounded below by an impermeable plane at an angle β to the horizontal (Figure 1). The coordinates axes are orthogonal with X aligned to steepest descent along the sloping boundary and Z perpendicular to the boundary. The steady flow thickness is given by $Z = H(X, Y)$. We assume throughout that the flow is "shallow"; the velocity in the Z direction is negligible relative to the velocity in the X and Y directions. Under this "lubrication" approximation, the excess pressure within the fluid is hydrostatic (Bear, 1971; Huppert & Woods, 1995),

$$P = \Delta\rho g\Big[H(X,Y) - Z\Big]\cos\beta, \tag{1}$$

where $\Delta\rho$ is the density difference between the intruding fluid and the ambient. The Darcy velocity is given by (Bear 1971; Vella and Huppert 2006):

$$\mathbf{U} = -\frac{K(R)\Delta\rho g}{\mu}\left(-\sin\beta + \cos\beta\frac{\partial H}{\partial X}, \cos\beta\frac{\partial H}{\partial Y}\right), \tag{2}$$

where $R = |\mathbf{X}|$ and the permeability of the medium, $K(R)$, may take different constant values inside and outside the cylinder, which is of radius L,

$$K(R) = \begin{cases} K_i, & R < L, \\ K_o, & R > L. \end{cases} \tag{3}$$

We analyze the injection of fluid at a constant flux per unit width, Q, from a line source far upstream. Away from the cylinder, the steady flow depth is a constant, given by Huppert and Woods (1995):

$$H_\infty = \frac{\mu\phi Q}{\Delta\rho g K_o \sin\beta}, \tag{4}$$

where ϕ is the porosity, assumed to be constant. In the case that the input fluid is the non-wetting phase (such as in CO_2 sequestration) there may be a significant "capillary entry pressure" that must be exceeded for the input fluid to invade regions of low permeability or porosity (Bachu, 2015; Bear & Ryzhik, 1998). This entry pressure is associated with the effects of interfacial tension between the fluids restricting flow through the pore throats and is approximately given by (Purcell 1949)

$$P_c = \frac{2\sigma\cos\alpha}{D}, \tag{5}$$

where D is the maximum pore throat radius, α is the contact angle and σ represents interfacial tension. The hydrostatic pressure at the edge of the cylinder must exceed P_c, which corresponds to the following condition on the flow depth (Woods & Farcas, 2009),

$$H > H_c = \frac{P_c}{\Delta\rho g\cos\beta}. \tag{6}$$

Typical values of the capillary entry pressure for low permeability shales in the context of CO_2 sequestration are $P_c = 0.5$–5 MPa (Chiquet et al., 2007; Kuila & Prasad, 2013; Rezaeyan et al., 2015), which with a density difference of 300 kgm^{-3} implies that the flow depth must exceed approximately $H_c = 300$ m. In Figure 1c, the maximum flow depth at the boundary of an impermeable cylinder relative to the upstream depth, $H_{\max}/H_\infty$ is plotted as a function of the flow parameter, $\mathcal{F}$ (defined below in [9]). Typical flows in subsurface aquifers have thicknesses of up to tens of meters and thus we anticipate that even given an increase in depth near the cylinder, inclusions of such low permeability are never invaded. In the calculations that follow, we examine the flow fields and thicknesses for inclusions that are of greater and smaller permeabilities than the surroundings, noting that if $H_{\max} < H_c$ then the inclusion may be modeled as impermeable.

We use the following scalings to non-dimensionalize the problem,

$$h = H \,/\, H_\infty, \qquad x = X \,/\, L, \qquad y = Y \,/\, L \quad \text{and} \quad r = R \,/\, L. \tag{7}$$

The dimensionless flux is simply the product of the in-plane velocities with the flow thickness, $\mathbf{q} = \int_0^h (u, v)\mathrm{d}z = (uh, vh)$, since u and v are independent of z. The flux may be expressed as

$$\mathbf{q} = k(r)h\left(1 - \mathcal{F}\frac{\partial h}{\partial x}, -\mathcal{F}\frac{\partial h}{\partial y}\right), \tag{8}$$

where $k(r) = 1$ in $r > 1$ and $k(r) = \lambda = K_i/K_o$ in $r < 1$. The dimensionless problem is governed by two parameters: the permeability ratio and the flow parameter;

$$\lambda = \frac{K_i}{K_o}, \qquad \mathcal{F} = \frac{H_\infty}{L\tan\beta}, \tag{9}$$

both of which may feasibly vary over a wide range of values. The flow parameter, $\mathcal{F}$, measures the thickness of the oncoming flow relative to the lengthscale of the cylindrical inclusion and the inclination of the underlying boundary. In this way it is the ratio of the flow driven by gradients of the hydrostatic pressure ($\Delta\rho g K \cos\beta H/[\mu L]$) to the flow driven by gravity downslope ($\Delta\rho g K \sin\beta/\mu$).

Since the flow is steady, mass conservation is given by requiring that the divergence of the flux (8) vanishes, which yields the following governing equation for the steady dimensionless flow depth, $h(x, y)$,

$$\frac{\partial h}{\partial x} = \mathcal{F}\nabla^2 h^2 \,/\, 2, \tag{10}$$

in both $r > 1$ and $r < 1$. On the cylinder boundary, the pressure and volume flux are continuous (provided that h is non-vanishing), which corresponds to

$$h^+ = h^-, \quad \text{and} \quad \cos\theta - \mathcal{F}\frac{\partial h}{\partial r}^+ = \lambda\left(\cos\theta - \mathcal{F}\frac{\partial h}{\partial r}\right), \tag{11}$$

where θ is the polar angle and $A^\pm$ denotes the value of A at $r = 1^\pm$. In the far-field, the flow depth returns to its uniform value ($h \to 1$ as $r \to \infty$).

In this study we integrate the system numerically and analyze it asymptotically to draw out the important behaviors. To solve the steady governing system numerically, we first reformulate it into a weak form. We multiply the equation for mass conservation, $\nabla\cdot\mathbf{q} = 0$, by a test function v and integrate over the domain, Ω, to obtain

$$\iint_\Omega k(r)h\left(1 - \mathcal{F}\frac{\partial h}{\partial x}, -\mathcal{F}\frac{\partial h}{\partial y}\right)\cdot\nabla v\mathrm{d}x\mathrm{d}y = \int_{x=L_2} k(r)hv\mathrm{d}S. \tag{12}$$

We have used a rectangular domain, $\Omega = [-L_1, L_2]\times[0, L_3]$, where $L_i > 0$ and we have exploited the symmetry about $y = 0$ to reduce computational effort. We have also deployed the following boundary conditions:

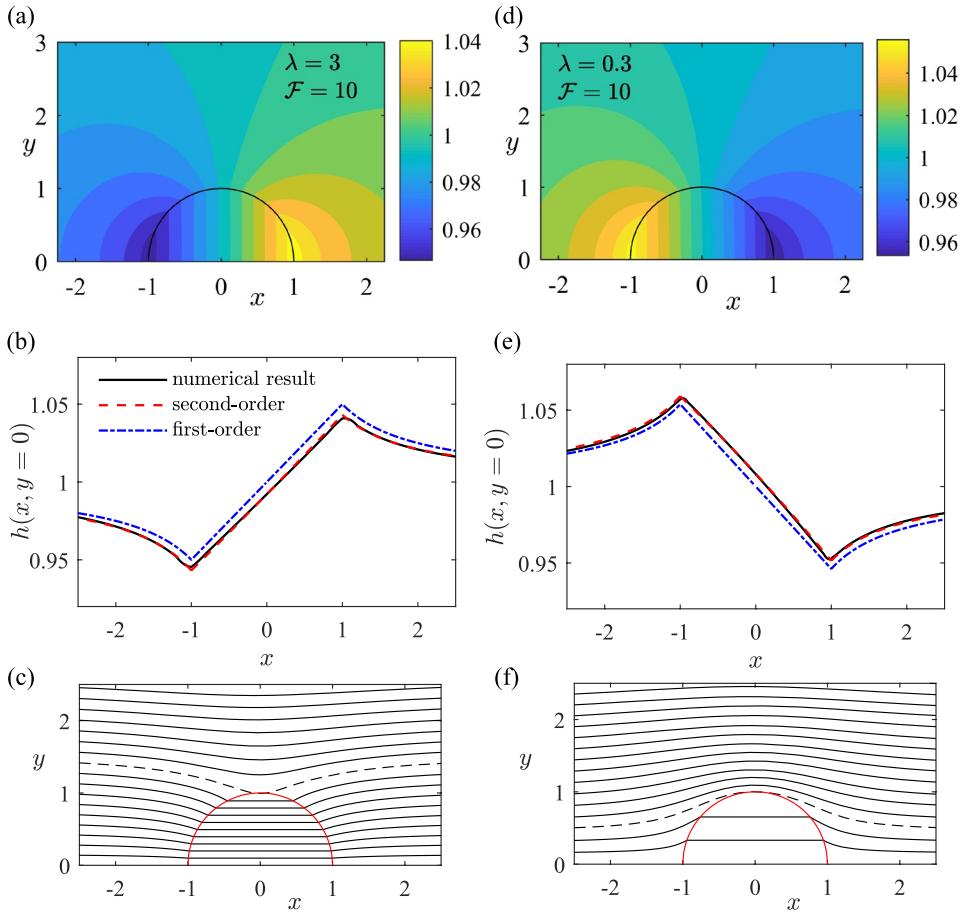

Figure 2. (a) Color plot of the thickness of the steady flow past a cylinder of relatively greater permeability, $\lambda = 3$, with $\mathcal{F} = 10$. (b) Flow thickness along the centerline, $y = 0$. (c) Particle paths through the cylinder from upstream. The dashed path just touches the cylinder. (d, e, f) Equivalent panels for $\lambda = 0.3$, with $\mathcal{F} = 10$.

$\partial h/\partial y = 0$ on $y = 0, L_3$, $\partial h/\partial x = 0$ on $x = L_2$ and $h = 1$ on $x = L_1$. This variational problem is solved in FEniCS, which uses numerical finite elements to compute the solution (Petter Langtangen & Logg, 2017). The steady state is found iteratively; we take an initial guess to be $h = 1$ everywhere, corresponding to the case $\lambda = 1$ and iterate until a converged solution is found. The domain size is increased until the solution becomes independent of further increases to it. Typical values are $L_1 = 10$, $L_2 = 30$, and $L_3 = 10$. In the following sections, we analyze the dynamics of the flow in different regimes for the relative magnitude of $\mathcal{F}$ and λ.

3. Relatively Narrow Cylinders ($\mathcal{F} \gg 1$)

To illustrate the solution for $\mathcal{F} \gg 1$ we plot the flow thickness for $\mathcal{F} = 10$ and two values of λ in Figures 2a and 2d. In the case that the cylinder is less permeable than the exterior, the flow is deeper upstream and shallower downstream whilst the converse occurs in the case that the cylinder is more permeable than the exterior. Figure 2 also suggests that the flow thickness within the cylinder is approximately independent of the cross-slope coordinate y. We explore these observations more formally using asymptotic analysis.

For a relatively deep oncoming flow, we expect the cylindrical inclusion of a different permeability to perturb the flow depth only weakly because the induced pressure gradients associated with any height anomalies lead to flows which reduce them and this effect dominates the motion down the inclined impermeable surface (see Figure 2). This motivates the expansion

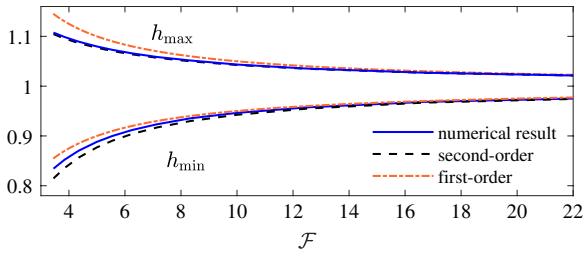

Figure 3. Maximum and minimum flow thickness for the steady flow through a cylinder of different permeability, with $\lambda = 3$. The asymptotic prediction (19) is plotted as a dashed line and the first order prediction, $h = 1 \pm \mathcal{F}^{-1} \mid 1 - \lambda \mid /(1 + \lambda)$ is plotted as a dot-dashed line.

$$h = 1 + \mathcal{F}^{-1} h_1 + \mathcal{F}^{-2} h_2 + \cdots \tag{13}$$

On substituting (13) into (10) and equating at $O(\mathcal{F}^{-1})$, we find that the equation governing h_1 is given by

$$\nabla^2 h_1 = 0 \tag{14}$$

with boundary conditions $h_1 \to 0$ as $r \to \infty$ and

$$h_1^+ = h_1^-, \qquad \text{and} \qquad \frac{\partial h_1}{\partial r}^+ - \lambda \frac{\partial h_1}{\partial r}^- = (1 - \lambda)\cos\theta, \quad \text{on} \quad r = 1, \tag{15}$$

where the superscripts $^+$ and $^-$ denote evaluation at $r = 1^+$ and 1^-, respectively. The solution is given by

$$h_1 = \frac{\lambda - 1}{\lambda + 1} \begin{cases} r\cos\theta & r < 1 \\ r^{-1}\cos\theta & r > 1. \end{cases} \tag{16}$$

The solution is anti-symmetric about the y axis, which can be observed in the plots of the numerical results in Figure 2. The flow depth predicted by the first-order expansion, $h = 1 + \mathcal{F}^{-1} h_1$, is compared with the numerical results along the centerline in Figures 2b and 2e. A less permeable cylinder ($\lambda < 1$) leads to an increase in the flow thickness upstream of the cylinder because flow is diverted around it. Conversely, a more permeable cylinder ($\lambda > 1$) leads to a decrease in flow thickness upstream of the cylinder because the flow is focused into the cylinder.

To determine the next term in the expansion (13), h_2, the solution in the region $r > 1$ requires matched asymptotic expansions to handle far-field divergences. The details are provided in the supplementary material, which adapts the method of Hinton et al. (2020). The inner solution, which is valid in $r < 1$, is given by

$$h_2 = \frac{\lambda - 1}{4(\lambda + 1)} \left\{ 2\gamma + 2\log[1 \,/\, (4\mathcal{F})] + \frac{r^2}{\lambda + 1}(2 + \cos 2\theta) \right\} \tag{17}$$

and in $r > 1$,

$$h_2 = \frac{\lambda - 1}{4(\lambda + 1)} \left\{ 2\gamma + 2\log[r \,/\, (4\mathcal{F})] + \frac{\lambda(1 - r^{-2})(1 + \cos 2\theta) + 1 + \cos 2\theta + r^{-2}}{\lambda + 1} \right\}, \tag{18}$$

where $\gamma = 0.577...$ is Euler's constant. The flow thickness predicted by our asymptotic expansions compares very favorably with the numerical results along the centerline with $\mathcal{F} = 10$ in Figure 2b for $\lambda = 3$ and Figure 2e for $\lambda = 0.3$.

If the cylindrical inclusion is less permeable than the surroundings ($\lambda < 1$) then the flow attains its maximum depth at $r = 1$ and $\theta = \pi$ and its minimum value at $r = 1$ and $\theta = 0$. The locations of the maxima and minima are interchanged for $\lambda > 1$. It is therefore possible to express the maxima and minima in compact form as

$$h_\pm = 1 \pm \mathcal{F}^{-1} \frac{\mid 1 - \lambda \mid}{1 + \lambda} + \mathcal{F}^2 \frac{\lambda - 1}{2(\lambda + 1)} \left[\gamma + \frac{3}{2(\lambda + 1)} - \log(4\mathcal{F}) \right]. \tag{19}$$

This expression compares very favorably with our numerical results for the minimum and maximum flow thickness (Figure 3, $\lambda = 3$). We note that the expansion (19) is valid for all λ even $\lambda \gg 1$ provided that $\mathcal{F} \gg 1$ because the magnitude of the expression $|1-\lambda|/(1 + \lambda)$, which occurs in the second and third terms of (19), is at most 1.

3.1. Particle Paths and Flux into the Cylinder

We use the results above to obtain the leading order velocity outside the cylinder ($r > 1$) for $\mathcal{F} \gg 1$,

$$\mathbf{u} = \left(1 + \frac{\lambda - 1}{\lambda + 1}\frac{\cos 2\theta}{r^2}, \frac{\lambda - 1}{\lambda + 1}\frac{\sin 2\theta}{r^2}\right) + \mathcal{O}\left(\mathcal{F}^{-1}\right), \tag{20}$$

whilst inside the cylinder,

$$\mathbf{u} = \left(\frac{2}{\lambda + 1}, 0\right) + \mathcal{O}\left(\mathcal{F}^{-1}\right). \tag{21}$$

Hence the total dimensionless flux into (and out of) the cylinder is

$$\frac{4\lambda}{\lambda + 1} + \mathcal{O}\left(\mathcal{F}^{-1}\right) \tag{22}$$

This flux vanishes for an impermeable cylinder ($\lambda = 0$), is equal to 2 for an equal permeability cylinder ($\lambda = 1$) and is at most 4 for a very permeable cylinder ($\lambda \to \infty$).

The particle paths to leading order for $\mathcal{F} \gg 1$ are shown in Figures 2c and 2f for $\lambda = 3$ and $\lambda = 0.3$. By considering the flux (22), we can determine that fluid in the interval $|y| < 2\lambda/(\lambda + 1)$ from far upstream enters the cylinder (this region is denoted by a dashed line in Figures 2c and 2f). The upstream region that is focused is at most $|y| < 2$ and hence particles outside this zone never pass through even the most permeable of cylinders.

Finally, we note that the leading order variation to the uniform depth, h_1, determines the perturbation to the hydrostatic pressure. Its governing equation is identical to the pressure field when the flow is driven in two-dimensions past a cylindrical inclusion by an imposed pressure difference (Bear, 1971).

4. Flow Through a Relatively Wide Cylinder ($\mathcal{F} \ll 1$, $\lambda = \mathcal{O}(1)$)

In the case of a relatively wide cylinder ($\mathcal{F} \ll 1$), qualitatively different behavior occurs depending on the relative permeability of the cylindrical inclusion. We find that there are three possible regimes, which correspond to $\lambda \ll 1$, $\lambda = \mathcal{O}(1)$ and $\lambda \gg 1$ (see the panels in Figure 4). In this section we analyze the middle case of similar permeabilities ($\lambda = \mathcal{O}(1)$). The flow is not significantly diverted by the cylinder and the velocity is equal to (1, 0) to leading order outside the cylinder and (λ, 0) inside the cylinder. The particle paths are nearly parallel to the x axis. Almost all the fluid emanating from $|y| < 1$ upstream flows into the cylinder. There is an abrupt change in the flow depth at $r = 1$ and this transition region is analyzed in §4.1. Then, in §4.2 we show that diversion at the cylinder boundary becomes important when the inclusion is of very low or very high permeability and these cases are analyzed in §5 and §6, respectively.

4.1. Asymptotic Analysis for Flow Through the Cylinder ($\lambda \sim 1$)

When a steady flow encounters a relatively wide cylindrical inclusion of similar permeability to the surrounding medium, mass conservation implies that the flow thickness inside the cylinder is $1/\lambda$ to leading order, while outside it is unity (see Figure 4a). A narrow zone occurs around the edge of the cylinder in which the thickness transitions from one value to another. To examine the depth here we introduce a rescaled radial coordinate, $\xi = (r - 1)\,/\,\mathcal{F}$ and write the flow depth interior and exterior to the cylinder as

$$h_{\text{int}} = h_{i0} + \mathcal{O}(\mathcal{F}), \qquad h_{\text{ext}} = h_{e0} + \mathcal{O}(\mathcal{F}). \tag{23}$$

The leading order terms in the governing equation are then given by

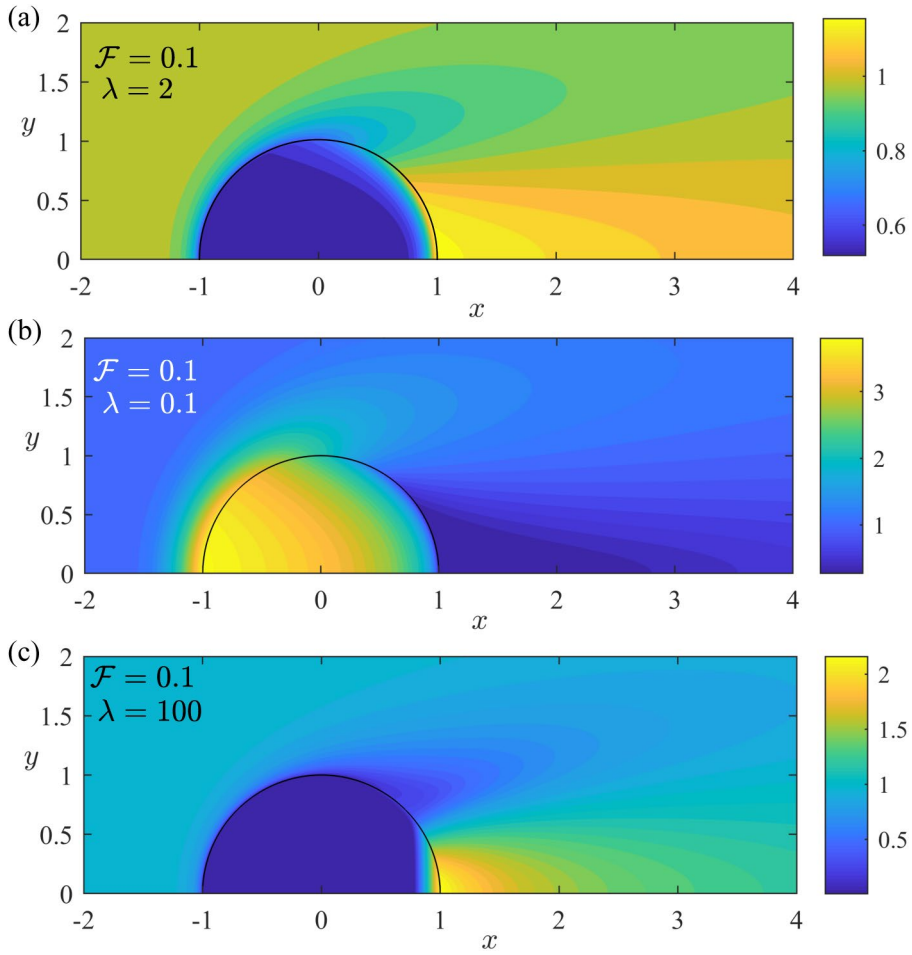

Figure 4. Thickness of the steady flow past a relatively wide cylindrical inclusion ($\mathcal{F} \ll 1$). The panels demonstrate the behavior in the three regimes analyzed in §§4, 5, and 6. Note the different colourscale in each plot.

$$\cos\theta \frac{\partial \hat{h}}{\partial \xi} = \frac{\partial}{\partial \xi}\left(\hat{h} \frac{\partial \hat{h}}{\partial \xi} \right), \tag{24}$$

where $\hat{h}$ denotes either h_{i0} or h_{e0}. Outside of the transition zone, the flow depth, $\hat{h}$, matches to a far field value, namely $h_{i0} \to 1/\lambda$ as $\xi \to -\infty$ and $h_{e0} \to 1$ as $\xi \to \infty$. Conditions at the edge of the cylinder require that

$$h_{i0} = h_{e0} \qquad \text{and} \qquad \cos\theta - \frac{\partial h_{e0}}{\partial \xi} = \lambda\left(\cos\theta - \frac{\partial h_{i0}}{\partial \xi} \right) \qquad \text{at} \quad \xi = 0. \tag{25}$$

We integrate (24) and apply the far-field conditions to find

$$\cos\theta(h_{e0} - 1) = h_{e0}\frac{\partial h_{e0}}{\partial \xi}, \qquad \text{and} \qquad \cos\theta(h_{i0} - 1/\lambda) = h_{i0}\frac{\partial h_{i0}}{\partial \xi}. \tag{26}$$

If $\cos\theta > 0$ (26a) requires that $h_{e0} = 1$ and then integrating (26b) and applying boundary conditions leads to

$$\xi\cos\theta = h_{i0} - 1 + \lambda^{-1}\log\left| \frac{h_{i0} - \lambda^{-1}}{1 - \lambda^{-1}} \right|. \tag{27}$$

Conversely if $\cos\theta < 0$ then we deduce that $h_{i0} = \lambda^{-1}$ and integrating (26a) yields

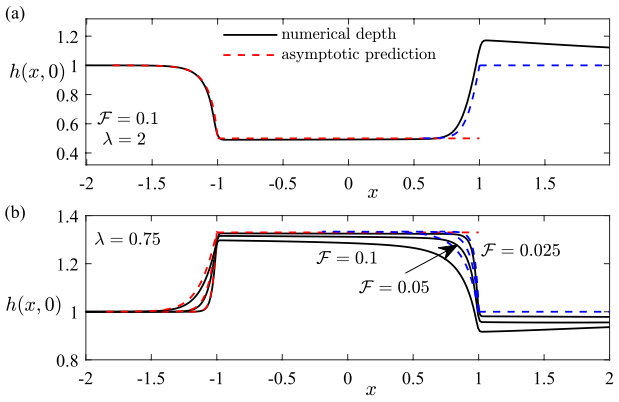

Figure 5. The steady flow thickness along the centerline for a relatively wide cylinder ($\mathcal{F} \ll 1$) with permeability of the same order of magnitude as the surrounding medium ($\lambda \sim 1$). The asymptotic predictions from §4.1 (red dashed lines upstream and blue dashed lines downstream) are compared to the numerical results (black lines). (a) $\lambda = 2$. (b) $\lambda = 0.75$.

$$\xi \cos\theta = h_{e0} - \lambda^{-1} + \log\left|\frac{h_{e0}-1}{\lambda^{-1}-1}\right|. \tag{28}$$

The leading order expansions obtained here for the flow depth are favorably compared to the numerical results along the centerline in Figure 5. A region in which the flow depth is deeper than predicted occurs at the downstream boundary in the case that $\lambda > 1$ (Figure 5a). For large enough permeability contrasts, this deep region invalidates the asymptotic analysis as discussed in the next subsection. A similar breakdown occurs at the upstream boundary in the case that the inclusion is of much lower permeability than the exterior.

4.2. Breakdown of the Asymptotic Analysis for Cylinders of Relatively Low and High Permeability

If the cylinder is of much lower permeability than the surrounding medium ($\lambda \ll 1$) then the gradient in the flow depth near $r = 1$, described above, is large (Figure 4b). There is a deep region upstream of but close to the cylinder in which the flow around the boundary of the cylinder becomes important. For sufficiently small λ, the flow into this deep region is balanced predominantly by flow around the cylinder rather than flow into the cylinder (see Figures 6a and 6b). In this case, the cylinder acts as an almost impermeable medium, an effect that might be accentuated by the inclusion of an entry pressure, and the asymptotic analysis in the preceding section is not valid. In the present subsection, we investigate how impermeable the cylinder needs to be, for a particular oncoming flow depth and cylinder width, for the flow to be predominantly diverted around the cylinder. Note that this diversion is also associated with increased flow thickness cross-stream of the cylinder in $1 < y < 1.5$ and decreased flow thickness

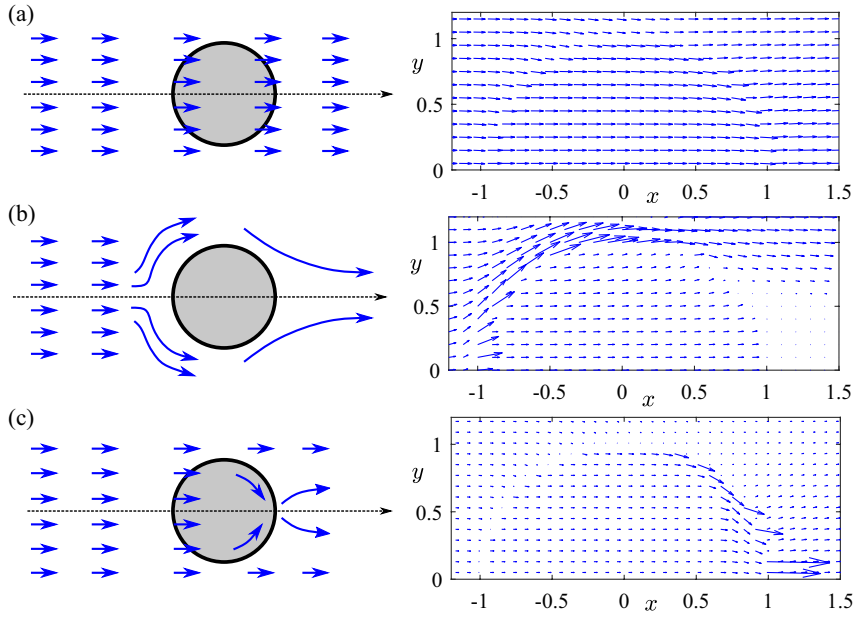

Figure 6. Schematics of the regimes for relatively shallow flow ($\mathcal{F} \ll 1$) past a circular cylindrical inclusion (left column) and corresponding plots of the flux vector, **q**, obtained numerically (right column). (a) Inclusion permeability similar to the exterior ($\mathcal{F}^{1/2} \ll \lambda \ll \mathcal{F}^{-1}$). The flow is predominantly parallel to the downslope direction. The case $\lambda = 2$, $\mathcal{F} = 0.2$ is shown on the right. (b) Inclusion of low permeability ($\lambda \ll \mathcal{F}^{1/2}$); the flow is predominantly diverted around the cylinder ($\lambda = 0.15$, $\mathcal{F} = 0.05$ is shown). (c) Inclusion of high permeability ($\lambda \gg \mathcal{F}^{-1}$); the flow is diverted at the downstream boundary toward the centerline where a deep pond of fluid develops ($\lambda = 50$, $\mathcal{F} = 0.2$ is shown).

downstream in $0 < y < 1$ (see Figure 4b).To obtain this relationship between $\mathcal{F}$ and λ at which the transition between Figures 6a and 6b occurs, we consider the flux around the cylinder predicted by the expansion for negligible diversion (28). Just upstream of but near to the cylinder ($\xi \ll 1$), the leading order flow depth can be obtained by linearizing (28),

$$h_{e0} = \lambda^{-1} + (1-\lambda)\xi\cos\theta, \tag{29}$$

which vanishes at $\xi = \overline{\xi}(\theta) = -1/[(1-\lambda)\lambda\cos\theta]$. The tangential flux around the cylinder in the region close to the cylinder ($\xi \ll 1$) to leading order is

$$\mathcal{F}\int_{\xi=0}^{\xi=\overline{\xi}(\theta)} -h_{e0}u_\theta \,\mathrm{d}\xi = \frac{-\lambda^{-2}\mathcal{F}\tan\theta}{2}, \tag{30}$$

since the leading order term in the tangential velocity is $u_\theta = -\sin\theta$ and we have assumed that $\lambda \ll 1$. For the "negligible" diversion regime to be self-consistent, the flux (30) must be much less than the flux into the cylinder, which is order 1, requiring $\mathcal{F}^{1/2} \ll \lambda$. Hence a transition occurs when $\lambda \sim \mathcal{F}^{1/2}$. The flow structure in the case of a relatively impermeable cylinder ($\lambda \ll \mathcal{F}^{1/2}$) is described in Section 5 (see also Figure 6b).

In the case that the cylinder is much more permeable than the surrounding medium, the analysis of the preceding section breaks down inside the cylinder near the downstream boundary. This is because the exterior is much less permeable and so the fluid within the cylinder is focused toward $x = 1, y = 0$ rather than flowing out of the cylinder along streamlines that are parallel to the downslope direction (see Figure 6c). The focusing is associated with a reduced flow depth downstream of the cylinder along $y \approx 1$ and an increased flow depth downstream of the cylinder along the centerline toward which the flow is diverted (see Figure 4c). To obtain the relationship between $\mathcal{F}$ and λ at which the transition to this high permeability regime occurs, we apply a similar flux argument to that described above.

According to the $\lambda \sim 1$ asymptotic analysis, the flow depth in the transition region inside the cylinder near the downstream boundary is given by Equation 27. For large λ, we linearize the depth in this region to obtain

$$h_{i0} = 1 + \xi\cos\theta. \tag{31}$$

This vanishes at $\xi = -1/\cos\theta$. The flux tangential to the boundary, just inside the cylinder is given by

$$\mathcal{F}\int_{\xi=1/\cos\theta}^{\xi=0} \lambda h_{i0}u_\theta \mathrm{d}\xi. \tag{32}$$

The leading order term in the velocity is $u_\theta = -\sin\theta$ and we calculate that the tangential flux is

$$\frac{-\lambda\mathcal{F}\tan\theta}{2}. \tag{33}$$

The asymptotic analysis in the previous subsection, where there is no diversion of the flow, is valid provided that this tangential flux is much smaller than the flux in the downslope direction, which is unity. In other words, there is no diversion provided that $\lambda\mathcal{F} \ll 1$ but if $\lambda \gg \mathcal{F}^{-1}$ then the exterior behaves as almost impermeable relative to the inclusion and a different asymptotic expansion is needed at the downstream boundary (see §6). We conclude the present section by noting that the "negligible" diversion behavior, as described above, occurs provided that $\mathcal{F}^{1/2} \ll \lambda \ll \mathcal{F}^{-1}$, which corresponds to a sufficiently shallow oncoming flow (or sufficiently wide cylinder) and permeabilities that are sufficiently similar.

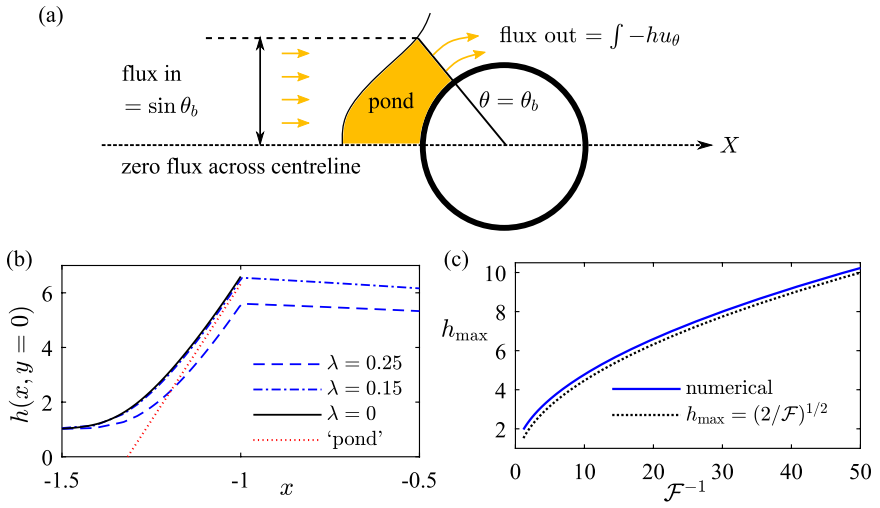

Figure 7. (a) Schematic illustrating the balance of flux in the pond. (b) Flow depth along the centerline for three values of λ with $\mathcal{F} = 0.05$. For $\lambda = 0$, the numerical solution was calculated using a no flux boundary condition at $r = 1$. The upstream asymptotic approximation (35) is shown in red dots. (c) Maximum flow thickness for the steady flow past an impermeable cylinder ($\lambda = 0$). The asymptotic approximation (39) is compared to the numerical results.

5. A Relatively Low Permeability Cylinder ($\lambda \ll \mathcal{F}^{1/2} \ll 1$)

We analyze the diversion of flow around a relatively wide cylindrical inclusion ($\mathcal{F} \ll 1$) that is of sufficiently low permeability relative to the exterior that the flux into the cylinder is negligible ($\lambda \ll \mathcal{F}^{1/2}$). We obtain the depth in $r > 1$ by assuming that the cylinder is impermeable to leading order. The flow outside the cylinder in the case of small but non-zero λ is similar to the flow for an impermeable cylinder ($\lambda = 0$), as demonstrated in Figure 7b.

Upstream of an impermeable cylinder, there is a "pond" of fluid in which the radial velocity is zero owing to the no-flux condition (see Hinton et al., 2019, 2020),

$$u_r = \cos\theta - \mathcal{F}\frac{\partial h}{\partial r} = 0. \tag{34}$$

Upon integrating we obtain the "pond" depth,

$$h_p = \mathcal{F}^{-1}(r-1)\cos\theta + g(\theta), \tag{35}$$

where $g(\theta)$ is a function of integration, which we determine by balancing the flux into and out of the pond (see Figure 7a). The pond vanishes ($h_p = 0$) at $r = r_0(\theta) = 1 - \mathcal{F}g(\theta)\,/\,\cos\theta > 1$. The flow depth returns to $h \sim 1$ here. The flux into the pond between $\theta = \pi$ and $\theta = \theta_b$ from upstream is $\sin\theta_b$ because the upstream flux is aligned with the x-axis and is unity, per unit width. The flux out of this region of the pond is provided by the tangential flux around the boundary at $\theta = \theta_b$,

$$\int_1^{r_0(\theta_b)} -hu_\theta \,\mathrm{d}r = \int_1^{r_0(\theta_b)} h_p \sin\theta_b \,\mathrm{d}r, \tag{36}$$

Where we have ignored the term $(\mathcal{F}\,/\,r)\partial h\,/\,\partial\theta$ in the velocity because it is negligible for $\mathcal{F} \ll 1$, which can be confirmed a posteriori. Balancing the fluxes and substituting in (35) yields

$$\sin\theta_b = \int_1^{r_0(\theta_b)} \Big[\mathcal{F}^{-1}(r-1)\cos\theta_b + g(\theta_b)\Big]\sin\theta_b \,\mathrm{d}r. \tag{37}$$

After some manipulation, we find that

$$g(\theta) = \mathcal{F}^{-1/2}(-2\cos\theta)^{1/2}. \tag{38}$$

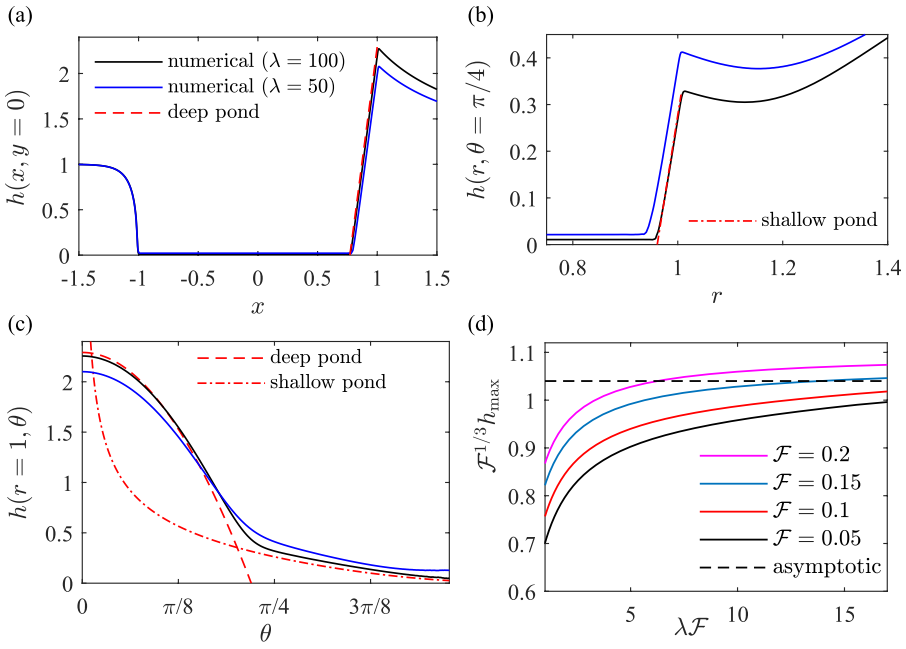

Figure 8. (a) Flow depth along the centerline with $\mathcal{F} = 0.1$. The asymptotic predictions are shown for $\lambda = 100$. (b) Flow depth along $\theta = \pi/4$. (c) Flow depth around the downstream boundary of the cylinder, $r = 1$, $0 < \theta < \pi/2$. (d) The maximum flow depth on rescaled axes. Numerical results for $\mathcal{F} = 0.05, 0.1, 0.15, 0.2$ are compared to the asymptotic prediction plotted as a dotted line (48).

The asymptotic prediction for the maximum flow depth, which occurs at $r = 1$, $\theta = \pi$, is given by

$$h_{\max} = 2^{1/2} \mathcal{F}^{-1/2}, \tag{39}$$

for $\mathcal{F} \ll 1$. We compare this expression (39) with the numerical results for the maximum flow thickness in Figure 7c. For $\lambda = 0$, a good empirical approximation for the maximum depth for all $\mathcal{F}$ is $h_{\max} = (1 + 2 \,/\, \mathcal{F})^{1/2}$ as shown in Figure 1c (c.f. Hinton et al., 2020).

The leading order expression for the flow depth along the centerline upstream of the cylinder ($x < 1$) is given by (35), which accurately reproduces the numerical results for $\mathcal{F} = 0.05$ in Figure 7b.

Finally, we comment on the validity of the lubrication model given that the flow has become relatively deep. Indeed the pond region has a large gradient in the free-surface but provided that $\tan\beta \ll 1$, the flow may still be approximated as shallow, for a full discussion see Lister (1992).

6. A Very Permeable Cylinder ($\lambda \gg \mathcal{F}^{-1} \gg 1$)

In the regime $\lambda \gg \mathcal{F}^{-1} \gg 1$, the flow is focused toward the downstream trailing edge of the cylinder ($x = 1$, $y = 0$), where a deep pond of fluid forms (see Figures 4c and 8a). The analysis of §4.1 is valid upstream in $x < 0$ (see Figure 8a). The regime transition occurs for large λ because the exterior acts as impermeable and a pond develops similar to the transition for small λ when the interior behaves as impermeable and a pond develops upstream in $r > 1$ (see Figures 6b and 6c).

We find that for $\lambda \gg \mathcal{F}^{-1}$, there is additionally a relatively "shallow" pond just upstream of the cylinder boundary and away from the centerline in which the boundary with the exterior appears impermeable. This corresponds to the spatial region $0 < 1 - r \ll 1$ and $\theta = \mathcal{O}(1) < \pi \,/\, 2$. We obtain the depth of this pond by balancing the flux from upstream with the flux tangential to the cylinder boundary. This shallow pond diverts fluid toward $x = 1$, $y = 0$, where there is a deeper pond, which we analyze by balancing the flux in from the shallow pond with the flux out of the cylinder.

We first analyze the flow thickness in the shallow pond. The exterior of the cylinder is approximately impermeable, which suggests that a ponded region forms in which the free surface is horizontal and given by

$$h_s = \mathcal{F}^{-1}(r-1)\cos\theta + m(\theta), \tag{40}$$

where $m(\theta)$ is a function that is to be determined. The region occupies

$$1 > r > r^*(\theta) = 1 - \mathcal{F}m(\theta) \,/\, \cos\theta. \tag{41}$$

We consider the flux balance in $(\theta, \pi/2)$. The flux from upstream within the cylinder into this region is $1-\sin\theta$. There is no flux out of the cylinder and balancing this upstream flux with the flux tangential to the cylinder boundary out of the region yields

$$1 - \sin\theta = \lambda \int_{r^*}^{1} h_s \sin\theta \,\mathrm{d}r \tag{42}$$

where we have ignored the lower order contribution to the tangential velocity, $(\mathcal{F} \,/\, r)\partial h \,/\, \partial\theta$, as it is negligible for $\mathcal{F} \ll 1$. Upon integrating and substituting for h_s, we obtain

$$m(\theta) = (\lambda\mathcal{F})^{-1/2} 2^{1/2} \left[(1-\sin\theta)\cot\theta\right]^{1/2}. \tag{43}$$

Note that in the corresponding expression in $-\pi/2 < \theta < 0$, the 1 is replaced by -1. The flow thickness in this pond is $h \sim (\lambda\mathcal{F})^{-1/2} \ll 1$. We note that the flux out of the cylinder in this region is $h\cos\theta$ to leading order owing to continuity at $r = 1$. Thus the flux leaving the inclusion is proportional to $(\lambda\mathcal{F})^{-1/2}$, which is much smaller than unity and consistent with the modeling assumption for this ponded region.

The pond prediction is compared to the numerical result for $\mathcal{F} = 0.1$ and $\lambda = 100$ along the ray $\theta = \pi/4$ in Figure 8b; the numerical result for $\lambda = 50$ is also included. The pond thickness is compared to the numerical result on the cylinder boundary ($r = 1$) in Figure 8c, which identifies that the present approximation is not accurate for $\theta \ll 1$. Indeed, $m(\theta)$ is singular as $\theta \to 0$. A second deeper pond approximation is needed here, which also accounts for the drainage of fluid out of the cylinder.

To quantify the size and depth of the deeper pond region localized to $x = 1$, $y = 0$ inside the cylinder, we again balance fluxes. The flow out of the cylinder occurs predominantly through this deeper pond region and the flux into the cylinder in $y \geq 0$ is unity. Thus the flux out of the deeper pond is also unity. The flow thickness in the pond is given by

$$h_d = \mathcal{F}^{-1}(x - x_0), \tag{44}$$

which corresponds to a horizontal free surface. The constant, x_0, is to be determined and we write $x_0 = \cos\theta_0$, where $\theta_0 \ll 1$ is the angular boundary of the pond region. The flux out of the pond is given by the radial flux just outside the cylinder at $r = 1^+$, which in the regime $\mathcal{F} \ll 1$ is given by

$$\int_0^{\theta_0} h_d \cos\theta \,\mathrm{d}\theta \tag{45}$$

at leading order, where we have used continuity of the thickness, h, at $r = 1$. Then balancing fluxes and integrating, we obtain

$$1 = \mathcal{F}^{-1}\left[\frac{\theta_0}{2} - \frac{\sin(2\theta_0)}{4}\right]. \tag{46}$$

Given that $\mathcal{F} \ll 1$, we expand to obtain $\theta_0 = 3^{1/3}\mathcal{F}^{1/3} + \mathcal{O}(\mathcal{F})$. The extent of the pond is given by

$$x_0 = \cos\theta_0 = 1 - (3^{2/3}/2)\mathcal{F}^{2/3} + \mathcal{O}(\mathcal{F}^{4/3}). \tag{47}$$

The maximum depth occurs at $x = 1, y = 0$ and is given by

$$h_{\max} = \frac{3^{2/3}}{2}\mathcal{F}^{-1/3} + \mathcal{O}(\mathcal{F}^{1/3}). \tag{48}$$

The prediction of the pond depth (44) shows good agreement with the numerical results along the centerline, $y = 0$, and along the cylinder boundary, $r = 1$, in Figures 8a and 8c with $\lambda = 100$ and $\mathcal{F} = 0.1$. We compare our prediction for the maximum depth (48) to the numerical results in Figure 8d. Each continuous line corresponds to a fixed value of $\mathcal{F}$, whilst λ is varied. The maximum flow depth becomes approximately independent of λ for $\lambda\mathcal{F} \gg 1$, in accord with our asymptotic theory. The error in $\mathcal{F}^{1/3}h_{\max}$ between asymptotic theory and the numerical results is a small fixed constant, proportional to $\mathcal{F}^{2/3}$, as $\lambda \to \infty$.

7. Cylinders With Non-Circular Cross-Sections

Hitherto, we have restricted our attention to circular cylinders. It is interesting to extend this analysis to other cross-sections to understand how the shape affects the depth of the steady flow. We focus on the case of a relatively wide cylinder ($\mathcal{F} \ll 1$). The calculation in the case of a relatively narrow cylinder ($\mathcal{F} \gg 1$) reduces to the problem of two-dimensional potential flow in order to determine the perturbation to the upstream flow depth, $h = 1 + \mathcal{F}^{-1}h_1$ (see §3).

7.1. Kite Cross-Section Cylinders

We analyze the interaction of the flow with a cylinder with a kite cross-section, symmetric about the centerline. The vertices are at $(0, \pm 1)$ and $(\pm\cot\psi, 0)$ and the kite edges make an angle ψ with the centerline. The general behavior is similar to the interaction with a circular cylinder and in what follows we highlight the key differences. For the regime in which there is little diversion of fluid ($\lambda \sim 1$), there are steep regions near the kite boundary within which the flow transitions from one depth to another, analogous to the behavior for a circular cylinder. We show below that the relative size of λ and $\mathcal{F}$ at the transitions between the three flow regimes are identical to the circular case by analyzing the high and low permeability regimes.

7.1.1. Relatively Low Permeability Cylinder ($\lambda \ll \mathcal{F}^{1/2}$)

We follow the argument for the low permeability circular cylinder and treat the interior as impermeable. A pond develops upstream of the upstream boundaries and we obtain its depth by balancing fluxes. We rotate coordinates with

$$x' = (x + \cot\psi)\cos\psi + y\sin\psi, \qquad y' = -x\sin\psi + y\cos\psi \tag{49}$$

In these coordinates, the upstream boundary lies along $0 < x' < 1/\sin\psi, y' = \cos\psi$.

The pond depth upstream of the kite can be written as

$$h_p = -\mathcal{F}^1(y' - \cos\psi)\sin\psi + G_R(x';\psi). \tag{50}$$

The flux balance in the pond is

$$x'\sin\psi = \int_{\cos\psi}^{\cos\psi + \mathcal{F}G_R/\sin\psi} h_p\cos\psi\,\mathrm{d}y' \tag{51}$$

and we obtain

$$G_R = \mathcal{F}^{-1/2}\left(\frac{2x'\sin^2\psi}{\cos\psi}\right)^{1/2}. \tag{52}$$

The flow depth increases with distance downstream along the wall, x', which contrasts with the case of a circular cylinder for which the maximum depth occurs at the upstream stagnation point. The scaling for the depth along the wall is $h \sim \mathcal{F}^{-1/2}$, which is identical to that for a circular cylinder. In fact, this scaling is obtained for any cylinder with non-zero curvature at the upstream point because the pond depth arises from the balance of the advective flux in with the advective flux out. The case of a perpendicular upstream boundary is analyzed in §7.2.

The maximum flow depth for the low permeability kite occurs near the cross-stream edge ($x' = 1/\sin\psi$) and is given by

$$h_{\max} = \left(2\tan\psi\right)^{1/2}\mathcal{F}^{-1/2}. \tag{53}$$

The flux into the inclusion in this regime is proportional to $\lambda\mathcal{F}^{-1/2}$ so the analysis is consistent provided that $\lambda \ll \mathcal{F}^{1/2}$. Also, the present analysis breaks down for ψ close to $\pi/2$ (see §7.2).

7.1.2. Relatively High Permeability Cylinder ($\lambda \gg \mathcal{F}^{-1}$)

In the case of a relatively high permeability ratio ($\lambda \gg \mathcal{F}^{-1}$), there is a shallow pond just upstream of the downstream boundary and away from the centerline. The depth there is of order $(\mathcal{F}\lambda)^{-1/2}$ as in the case of a circular cylinder because the balance is the same. The flux out of the cylinder away from the centerline is proportional to $(\mathcal{F}\lambda)^{-1/2}$, which is small provided that $\lambda \gg \mathcal{F}^{-1}$.

The deep pond near the centerline has depth $h = \mathcal{F}^{-1}(x - x_0)$. At the downstream boundary we rotate coordinates with

$$\hat{x} = (x - \cot\psi)\cos\psi - y\sin\psi, \qquad \hat{y} = x\sin\psi + y\cos\psi \tag{54}$$

In these coordinates, the downstream boundary lies along $1/\sin\psi < \hat{x} < 0$, $\hat{y} = \cos\psi$. The pond depth is given by

$$h = \mathcal{F}^{-1}(\hat{x}\cos\psi + \hat{x}_0\cos\psi) \tag{55}$$

The flux out of the cylinder is given by

$$\int_{-\check{x}_0}^{0} \mathcal{F}^{-1}(\check{x}\cos\psi + \check{x}_0\cos\psi)\sin\psi\,\mathrm{d}\check{x} = 1. \tag{56}$$

We integrate and obtain $\hat{x}_0 = (2\mathcal{F})^{1/2}(\sin\psi)^{-1/2}$ and the maximum flow depth is

$$\mathcal{F}^{-1/2}2^{1/2}(\sin\psi)^{-1/2}\cos\psi \tag{57}$$

Note the different depth scaling to the circular cylinder for which $h \sim \mathcal{F}^{1/3}$ (see (48)). In fact, the depth scaling in the deep pond is sensitive to the detailed shape (unlike the scaling upstream of a relatively impermeable cylinder).

In the shallow pond, the flow depth is

$$h = \mathcal{F}^{-1}\hat{y}\sin\psi + (\lambda\mathcal{F})^{-1/2}(\hat{x} + 1/\sin\psi)^{1/2}\left(\frac{2\sin^2\psi}{\cos\psi}\right)^{1/2} \tag{58}$$

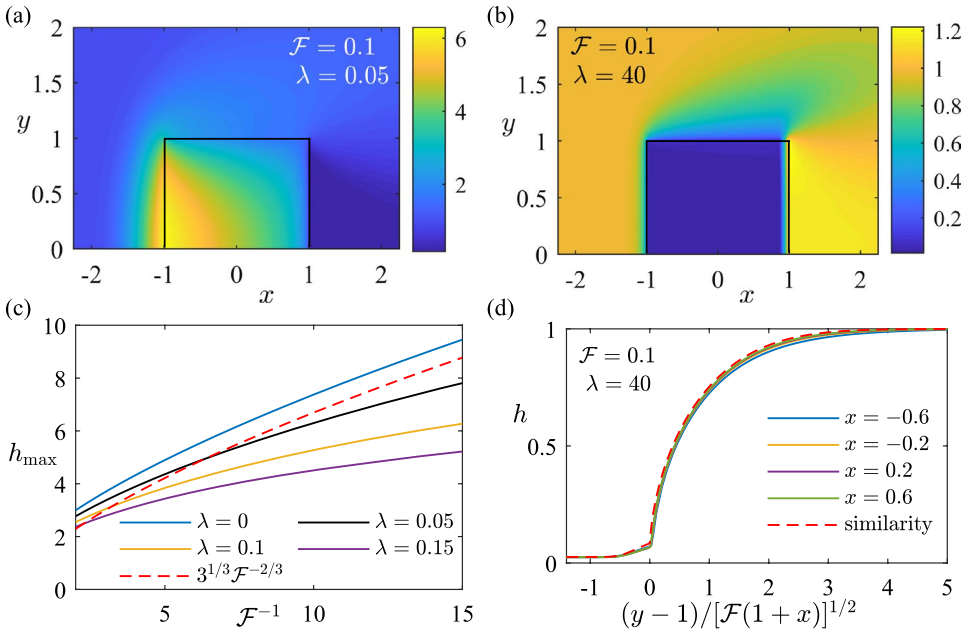

Figure 9. (a) and (b) Color plots of the thickness of the steady flow past a square cross-section inclusion (note the different depth scales). (c) The maximum flow thickness for low permeability square inclusions. (d) The self-similar behavior in the cross-sectional flow depth near the cross-stream boundary of the square ($y = 1$) for $\lambda = 40$.

which has the same scaling as the circular cylinder. This scaling occurs for any downstream boundary that is not perpendicular to the centerline.

7.2. Square Cross-Section Cylinders

We consider a square cylinder occupying $-1 < x < 1$, $-1 < y < 1$. Plots of the steady flow thickness are shown in Figure 9. In the case that there is little diversion of fluid, ($\lambda \sim 1$), there is a thin transition region, similar to that for a circular cylinder, near the upstream and downstream boundaries of the square.

7.2.1. Relatively Low Permeability Cylinder ($\lambda \ll \mathcal{F}^{2/3}$)

The main difference to the circular case is that the flux out of the upstream pond arises from terms associated with hydrostatic pressure gradients (which are proportional to $\mathcal{F}$) rather than from the advective flux associated with gravity acting downslope. This is because the boundary is perpendicular to the slope direction. We treat the interior of the square as impermeable. The pond depth is given by $h = \mathcal{F}^{-1}(x+1) + G_s(y)$. The flux balance in the pond is

$$1 = \frac{\partial}{\partial y}\left(\int_{\hat{x}}^{1} -\mathcal{F} h \frac{\partial h}{\partial y} \mathrm{d}x \right), \tag{59}$$

where $\hat{x} = -1 - \mathcal{F}G_s(y)$. We note that $G_s(1) = 0$ and $G_s'(0) = 0$ owing to the end of the pond at the corner of the square and symmetry about the centerline, respectively. This yields the following expression

$$G_s(y) = \mathcal{F}^{-2/3}\left[3(1-y^2)\right]^{1/3}, \tag{60}$$

which is a different scaling for the flow depth to the low permeability circular cylinder. The prediction for the maximum flow thickness is $h_{\max} = 3^{1/3}\mathcal{F}^{-2/3}$, which is compared to the numerical results in Figure 9c. The square cylinder behaves as impermeable for $\lambda \ll \mathcal{F}^{2/3}$ (note the difference with the circular case).

7.2.2. Relatively High Permeability Cylinder

In the case that the square cylinder is of much higher permeability than the exterior, the negligible diversion regime described above, in which the flow is approximately parallel to the centerline, applies. This is in contrast to the behavior for circular and kite cross-sections, where the behavior associated with negligible diversion breaks down at high permeability ratios because the flow in the direction tangential to the downstream boundary becomes significant. However, for a square cross-section, the downstream boundary is perpendicular to the slope direction and a permeability contrast does not give rise to cross-slope flow here. Hence there is no distinct high permeability regime for the square and the negligible diversion results apply provided that $\lambda \gg \mathcal{F}^{2/3}$. This is demonstrated in Figure 9b, where we have used $\lambda = 40$ and $\mathcal{F} = 0.1$ but the flow depth is ∼1 at the downstream boundary.

At the cross-stream boundaries $y = \pm 1$, there is a transition in the depth from the interior value, $h = \lambda^{-1}$, to the exterior value, $h = 1$. Away from the corners at $x = \pm 1, y = 1$ (by a distance of greater order than $\mathcal{F}$), the motion is controlled by a balance of downslope advection and cross-slope diffusion. Therefore, the governing equation in the transition region around $y = 1$ is approximately,

$$\frac{\partial h}{\partial x} = \mathcal{F}\frac{\partial}{\partial y}\left(h\frac{\partial h}{\partial y}\right), \tag{61}$$

in $y > 1$ and $y < 1$ with boundary conditions of continuity of h and a jump in $\partial h/\partial y$ associated with λ at $y = 1$. This has a similarity solution with $\eta = (y-1)\,/\,[\mathcal{F}(1+x)]^{1/2}$ with $h(\eta)$ satisfying

$$-\frac{1}{2}\eta\frac{\partial h}{\partial \eta} = \frac{\partial}{\partial \eta}\left(h\frac{\partial h}{\partial \eta}\right), \tag{62}$$

subject to continuity of h and $\lambda\partial h/\partial\eta^{-} = \partial h/\partial\eta^{+}$ at $\eta = 0$. We note that this self-similar transition behavior also occurs in the "negligible" diversion regime ($\lambda \sim 1$). The system (62) is integrated numerically and is compared to the numerical results in Figure 9d for $\lambda = 40$, demonstrating that the flow depth is approximately self-similar near the cross-stream boundary.

8. Discussion and Application

We recall the two dimensionless parameters that govern the flow: $\lambda = K_i/K_o$ and $\mathcal{F} = H_\infty\,/\,(L\tan\beta)$. In the case that the cylinder is relatively narrow ($\mathcal{F} \gg 1$), the dimensionless flux into the cylinder is $4\lambda/(\lambda+1)$. The corresponding dimensional flux is

$$\frac{4K_i}{K_i + K_o}LQ. \tag{63}$$

The flux (63) is independent of the upstream depth, H_∞ and the slope gradient, $\tan\beta$ (provided that $L \ll H_\infty/\tan\beta$) unlike the regime $\mathcal{F} \ll 1$. The particle paths are also independent of H_∞ and $\tan\beta$. This surprising result is related to the analogy between the $\mathcal{F} \gg 1$ regime and the case of pressure driven flow (for which there is no free-surface) described in §3.

We consider the common interaction between a CO_2 plume and an abandoned well (which may have been used for hydrocarbon recovery). We take the following typical parameters: well radius of $L = 0.25$ m, the permeability increases by a factor $\lambda = 1{,}000$, the upstream plume thickness is $H_\infty = 3$ m and the slope gradient is $\tan\beta = 0.01$ (Celia et al., 2005). This yields $\mathcal{F} = 1200$. We calculate that the flow depth varies by

less than a centimeter and fluid is drawn in from an upstream region of width 1 m. Thus the depth is very slightly changed by the well but the particle paths are strongly diverted.

For a relatively wide cylinder ($\mathcal{F} \ll 1$), there are three sub-regimes depending on the permeability ratio, λ. For large permeability contrasts, ponds accumulate at either the downstream or upstream boundary. For example, consider a rectangular inclusion of cross-stream width $L = 200$ m and much smaller permeability than the surroundings so that effectively $\lambda = 0$, (e.g. Figure 9 of Boggs et al., 1992; Di Donato & Blunt, 2004; Fitch et al., 2015). Suppose that the inclusion is in a CO_2 storage site where the upstream depth is $H_\infty = 1$ m and the slope is $\tan\beta = 0.02$. This inclusion may only be a few meters thick in the z direction. We calculate $\mathcal{F} = 0.25$. The depth increases to ∼4 m upstream of the inclusion. If instead the inclusion had twice the permeability of the exterior ($\lambda = 2$), then the depth within it would be ∼0.5 m near its upstream boundary but would gradually return to 1 m further downstream as fluid from the exterior flows across the sides of the inclusion.

9. Conclusion

We have analyzed the interaction of a gravitationally driven free-surface flow in an inclined porous medium with a cylindrical inclusion of different permeability to the exterior. In the case that the cylinder is relatively narrow ($\mathcal{F} \gg 1$), we have obtained expressions for the flux into the cylinder and the particle paths, which may be strongly diverted or focused by the cylinder even though the free-surface is only weakly perturbed.

For relatively wide inclusions ($\mathcal{F} \ll 1$), we have found three qualitatively different regimes depending on the ratio, λ, of the internal and external permeabilities. In the case that the permeabilities are similar ($\lambda \sim 1$), the flow is everywhere parallel to the downstream direction. The flow thickness takes two approximately constant values inside and outside the cylinder owing to mass conservation. The flow transitions in small regions adjacent to the cylinder boundary. We have shown that the flow in the upstream transition zone diverts more flow around than into the cylinder when the cylinder is of lower permeability, $\lambda \ll \mathcal{F}^{1/2}$. The cylinder appears almost impermeable and a deep pond of fluid forms upstream with a horizontal free-surface and depth $h \sim \mathcal{F}^{-1/2}$. This scaling is general to cylinders with non-zero curvature at the upstream stagnation point. For the case of a square cylinder, the scaling for the depth in this pond is $h \sim \mathcal{F}^{-2/3}$ instead.

The third regime for shallow oncoming flow occurs in the case of a high permeability cylinder. The transition away from the first regime is analogous to that for a low permeability cylinder; the flux tangential to the downstream boundary just inside the cylinder exceeds the flux out of the cylinder when $\lambda \gg \mathcal{F}^{-1}$. The flow is focused toward the rear side of the cylinder and there forms a pond of fluid within the cylinder at the rear. The flux out of the cylinder arises predominantly from the flow into and out of this pond. Interestingly, the flow depth in the pond becomes independent of the permeability contrast λ, when the latter is sufficiently large. Also, the flow depth in the pond is sensitive to the shape of the inclusion. Indeed, for a downstream boundary shape of the form $y = (1 - x)^{1/n}$ the deep pond has maximum depth $h \sim \mathcal{F}^{-a}$ where $a = -1/(1 + n)$. A kite corresponds to the case $n = 1$ and a circle corresponds to $n = 2$.

Our results provide insight into which of the various physical effects dominate in the interaction of free-surface porous flows with a single inclusion. It would be interesting to extend the analysis to an array of inclusions. Also, further study could focus on the transient evolution to the steady state such as investigating the role of capillary effects at the invading front and calculating the time taken for the inclusion to be filled with fluid. Finally, the model presented here may be straightforwardly adapted to include the effect of vertical leakage from within the inclusion through the underlying low permeability seal layer. This is manifest by an expression for mass loss in (10) associated with leakage driven by the hydrostatic pressure (Acton et al., 2001; Neufeld et al., 2011; Pritchard & Hogg, 2002). We briefly comment that in this scenario for relatively narrow cylinders ($\mathcal{F} \gg 1$), the flow depth is not changed at leading order; it is still given by $h = 1 + \mathcal{F}^{-1}h_1$, although h_1 takes a different form. For relatively wide cylinders, the maximum vertical leakage flux out of the cylinder is bounded above by the flux into the cylinder from the calculations described in this study.

Data Availability Statement

This article has no additional data.

Acknowledgments
E. M. Hinton is grateful to the London Mathematical Society and the Heilbronn Institute for Mathematical Research for the award of an Early Career Research Fellowship (ref: ECF-1920-82).

References

Acton, J. M., Huppert, H. E., & Worster, M. G. (2001). Two-dimensional viscous gravity currents flowing over a deep porous medium. *Journal of Fluid Mechanics*, *440*, 359–380. https://doi.org/10.1017/S0022112001004700

Bachu, S. (2015). Review of CO2 storage efficiency in deep saline aquifers. *International Journal of Greenhouse Gas Control*, *40*, 188–202. https://doi.org/10.1016/j.ijggc.2015.01.007

Barlow, P. M., & Reichard, E. G. (2010). Saltwater intrusion in coastal regions of north America. *Hydrogeology Journal*, *18*(1), 247–260. https://doi.org/10.1007/s10040-009-0514-3

Bear, J. (1971). *Dynamics of flow in porous media*. Elsevier

Bear, J., & Ryzhik, V. (1998). On the displacement of NAPL lenses and plumes in a phreatic aquifer. *Transport in Porous Media*, *33*(3), 227–255. https://doi.org/10.1023/A:1006544629038

Boggs, J. M., Young, S. C., Beard, L. M., Gelhar, L. W., Rehfeldt, K. R., & Adams, E. E. (1992). Field study of dispersion in a heterogeneous aquifer: 1. Overview and site description. *Water Resources Research*, *28*(12), 3281–3291. https://doi.org/10.1029/92WR01756

Celia, M., Bachu, S., Nordbotten, J., Gasda, S., & Dahle, H. (2005). Quantitative estimation of CO2 leakage from geological storage: Analytical models, numerical models, and data needs. *Greenhouse Gas Control Technologies*, *7*, 663–671. https://doi.org/10.1016/B978-008044704-9/50067-7

Chiquet, P., Daridon, J.-L., Broseta, D., & Thibeau, S. (2007). CO2/water interfacial tensions under pressure and temperature conditions of CO2 geological storage. *Energy Conversion and Management*, *48*(3), 736–744. https://doi.org/10.1016/j.enconman.2006.09.011

Dagan, G. (1984). Solute transport in heterogeneous porous formations. *Journal of Fluid Mechanics*, *145*, 151–177. https://doi.org/10.1017/S0022112084002858

Dagan, G., & Zeitoun, D. G. (1998). Free-surface flow toward a well and interface upconing in stratified aquifers of random conductivity. *Water Resources Research*, *34*(11), 3191–3196. https://doi.org/10.1029/98WR02039

Di Donato, G., & Blunt, M. J. (2004). Streamline-based dual-porosity simulation of reactive transport and flow in fractured reservoirs. *Water Resources Research*, *40*(4). https://doi.org/10.1029/2003WR002772

Eames, I., & Bush, J. W. M. (1999). Longitudinal dispersion by bodies fixed in a potential flow. *Proceedings of the Royal Society of London A*, *455*(1990), 3665–3686. https://doi.org/10.1098/rspa.1999.0471

Fitch, P. J. R., Lovell, M. A., Davies, S. J., Pritchard, T., & Harvey, P. K. (2015). An integrated and quantitative approach to petrophysical heterogeneity. *Marine and Petroleum Geology*, *63*, 82–96. https://doi.org/10.1016/j.marpetgeo.2015.02.014

Guo, B., Zheng, Z., Bandilla, K. W., Celia, M. A., & Stone, H. A. (2016). Flow regime analysis for geologic CO2 sequestration and other subsurface fluid injections. *International Journal of Greenhouse Gas Control*, *53*, 284–291. https://doi.org/10.1016/j.ijggc.2016.08.007

Hannis, S., Chadwick, A., Jones, D., Pearce, J., White, J., Connelly, D., et al. (2015). *Review of offshore monitoring for CCS projects*. IEAGHG.

Hewitt, D. R., Peng, G. G., & Lister, J. R. (2020). Buoyancy-driven plumes in a layered porous medium. *Journal of Fluid Mechanics*, *883*. https://doi.org/10.1017/jfm.2019.888

Hinch, E. J., & Bhatt, B. S. (1990). Stability of an acid front moving through porous rock. *Journal of Fluid Mechanics*, *212*, 279–288. https://doi.org/10.1017/S0022112090001963

Hinton, E. M., Hogg, A. J., & Huppert, H. E. (2019). Interaction of viscous free-surface flows with topography. *Journal of Fluid Mechanics*, *876*, 912–938. https://doi.org/10.1017/jfm.2019.588

Hinton, E. M., Hogg, A. J., & Huppert, H. E. (2020). Viscous free-surface flows past cylinders. *Physical Review Fluids*, *5*(8), 084101. https://doi.org/10.1103/PhysRevFluids.5.084101

Hinton, E. M., & Woods, A. W. (2019). The effect of vertically varying permeability on tracer dispersion. *Journal of Fluid Mechanics*, *860*, 384–407. https://doi.org/10.1017/jfm.2018.891

Huppert, H. E., & Woods, A. W. (1995). Gravity-driven flows in porous layers. *Journal of Fluid Mechanics*, *292*, 55–69. https://doi.org/10.1017/S0022112095001431

Kuila, U., & Prasad, M. (2013). Specific surface area and pore-size distribution in clays and shales. *Geophysical Prospecting*, *61*(2-Rock Physics for Reservoir Exploration, Characterisation and Monitoring), 341–362. https://doi.org/10.1111/1365-2478.12028

Lister, J. R. (1992). Viscous flows down an inclined plane from point and line sources. *Journal of Fluid Mechanics*, *242*, 631–653. https://doi.org/10.1017/S0022112092002520

MacFarlane, D. S., Cherry, J. A., Gillham, R. W., & Sudicky, E. A. (1983). Migration of contaminants in groundwater at a landfill: A case study: 1. Groundwater flow and plume delineation. *Journal of Hydrology*, *63*(1–2), 1–29. https://doi.org/10.1016/0022-1694(83)90221-4

Masterson, J. P., Walter, D. A., & LeBlanc, D. R. (1998). *Delineation of contributing areas to selected public-supply wells*. (Vol. 98). US Department of the Interior, US Geological Survey.

Mathieson, A., Midgely, J., Wright, I., Saoula, N., & Ringrose, P. (2011). In Salah CO2 Storage JIP: CO2 sequestration monitoring and verification technologies applied at Krechba, Algeria. *Energy Procedia*, *4*, 3596–3603. https://doi.org/10.1016/j.egypro.2011.02.289

Neufeld, J. A., Vella, D., Huppert, H. E., & Lister, J. R. (2011). Leakage from gravity currents in a porous medium. Part 1. A localized sink. *Journal of Fluid Mechanics*, *666*, 391–413. https://doi.org/10.1017/S002211201000488X

Nordbotten, J. M., Celia, M. A., & Bachu, S. (2004). Analytical solutions for leakage rates through abandoned wells. *Water Resources Research*, *40*(4). https://doi.org/10.1029/2003WR002997

Petter Langtangen, H., & Logg, A. (2017). *Solving PDEs in python: The FEniCS tutorial I*. Springer. https://doi.org/10.1007/978-3-319-52462-7

Phillips, O. M. (1991). *Flow and reactions in permeable rocks*. Cambridge University Press.

Pritchard, D. (2007). Gravity currents over fractured substrates in a porous medium. *Journal of Fluid Mechanics*, *584*, 415–431. https://doi.org/10.1017/S0022112007006623

Pritchard, D., & Hogg, A. J. (2002). Draining viscous gravity currents in a vertical fracture. *Journal of Fluid Mechanics*, *459*, 207–216. https://doi.org/10.1017/S0022112002008327

Purcell, W. R. (1949). Capillary pressures—Their measurement using mercury and the calculation of permeability therefrom. *Journal of Petroleum Technology*, *1*(02), 39–48. https://doi.org/10.2118/949039-G

Rezaeyan, A., Tabatabaei-Nejad, S. A., Khodapanah, E., & Kamari, M. (2015). A laboratory study on capillary sealing efficiency of Iranian shale and anhydrite caprocks. *Marine and Petroleum Geology*, *66*, 817–828. https://doi.org/10.1016/j.marpetgeo.2015.07.022

Sahu, C. K., & Flynn, M. R. (2017). The effect of sudden permeability changes in porous media filling box flows. *Transport in Porous Media*, *119*(1), 95–118. https://doi.org/10.1007/s11242-017-0875-3

Sekhar, G. P. R., & Sano, O. (2001). Two-dimensional viscous flow past a slightly deformed circular cavity in a porous medium. *Fluid Dynamics Research*, *28*(4), 281. https://doi.org/10.1016/S0169-5983(00)00033-2

Stalker, L., Boreham, C., Underschultz, J., Freifeld, B., Perkins, E., Schacht, U., & Sharma, S. (2015). Application of tracers to measure, monitor and verify breakthrough of sequestered CO2 at the CO2CRC Otway project, Victoria, Australia. *Chemical Geology*, *399*, 2–19. https://doi.org/10.1016/j.chemgeo.2014.12.006

Vella, D., & Huppert, H. E. (2006). Gravity currents in a porous medium at an inclined plane. *Journal of Fluid Mechanics*, *555*, 353–362. https://doi.org/10.1017/S0022112006009578

Werth, C. J., Cirpka, O. A., & Grathwohl, P. (2006). Enhanced mixing and reaction through flow focusing in heterogeneous porous media. *Water Resources Research*, *42*(12). https://doi.org/10.1029/2005wr004511

Woods, A. W., & Farcas, A. (2009). Capillary entry pressure and the leakage of gravity currents through a sloping layered permeable rock. *Journal of Fluid Mechanics*, *618*, 361–379. https://doi.org/10.1017/S0022112008004527

Woods, A. W., & Norris, S. (2010). On the role of caprock and fracture zones in dispersing gas plumes in the subsurface. *Water Resources Research*, *46*(8). https://doi.org/10.1029/2008WR007568